

Precipitation Forecasting Using Doppler Radar Data, a Cloud Model with Adjoint, and the Weather Research and Forecasting Model: Real Case Studies during SoWMEX in Taiwan

SHENG-LUN TAI AND YU-CHIENG LIOU

Department of Atmospheric Sciences, National Central University, Zhongli City, Taiwan

JUANZHEN SUN

National Center for Atmospheric Research, Boulder, Colorado

SHAO-FAN CHANG AND MIN-CHAO KUO

Department of Atmospheric Sciences, National Central University, Zhongli City, Taiwan

(Manuscript received 11 February 2011, in final form 23 April 2011)

ABSTRACT

The quantitative precipitation forecast (QPF) capability of the Variational Doppler Radar Analysis System (VDRAS) is investigated in the Taiwan area, where the complex topography and surrounding oceans pose great challenges to accurate rainfall prediction. Two real cases observed during intensive operation periods (IOPs) 4 and 8 of the 2008 Southwest Monsoon Experiment (SoWMEX) are selected for this study. Experiments are first carried out to explore the sensitivity of the retrieved fields and model forecasts with respect to different background fields. All results after assimilation of the Doppler radar data indicate that the principal kinematic and thermodynamic features recovered by the VDRAS four-dimensional variational data assimilation (4DVAR) technique are rather reasonable. Starting from a background field generated by blending ground-based in situ measurements (radiosonde and surface mesonet station) and reanalysis data over the oceans, VDRAS is capable of capturing the evolution of the major precipitation systems after 2 h of simulation. The model QPF capability is generally comparable to or better than that obtained using only in situ observations or reanalysis data to prepare the background fields. In a second set of experiments, it is proposed to merge the VDRAS analysis field with the Weather Research and Forecasting Model (WRF), and let the latter continue with the following model integration. The results indicate that through this combination, the performance of the model QPF can be further improved. The accuracy of the predicted 2-h accumulated rainfall turns out to be significantly higher than that generated by using VDRAS or WRF alone. This can be attributed to the assimilation of meso- and convective-scale information, embedded in the radar data, into VDRAS, and to better treatment of the topographic effects by the WRF simulation. The results illustrated in this study demonstrate a feasible extension for the application of VDRAS in other regions with similar geographic conditions and observational limitations.

1. Introduction

Doppler radar is capable of probing the atmosphere with high temporal (<10 min) and spatial resolution (<1.0 km), thereby providing a detailed description of the airflow structures inside a meso- or convective-scale weather system. During the past a few decades, numerous

methods have been developed for the purpose of improving weather forecast accuracy by assimilating radar data into a numerical model. Gal-Chen (1978) first showed that the thermodynamic parameters (i.e., pressure and temperature) can be inferred from the radar-derived three-dimensional winds, and these fields play an important role in correctly initializing a numerical model. There have been numerous studies conducted based on this concept to investigate the improvements one can achieve through the inclusion of radar data (e.g., Lin et al. 1993; Crook 1994; Crook and Tuttle 1994; Weygandt et al. 2002; Zhao et al. 2006). The three-dimensional variational

Corresponding author address: Dr. Yu-Chieng Liou, Dept. of Atmospheric Sciences, National Central University, 320, Zhongli City, Taiwan.
E-mail: tyliou@atm.ncu.edu.tw

data assimilation (3DVAR) technique has also been adopted to explore the impacts of assimilating Doppler velocities on forecasts of severe weather events. Some examples are the heavy rainfall associated with a cold front in the Korean Peninsula (Xiao et al. 2005), a squall line observed in the International H₂O Project (IHOP; Xiao and Sun 2007), tornadic thunderstorms in Texas (Hu et al. 2006a,b), and a strong long-lasting convective storm near Montreal, Quebec, Canada (Chung et al. 2009). Recently, active research has been undertaken to apply the ensemble Kalman filter (EnKF) technique for assimilating Doppler as well as dual-polarimetric radar observations (Snyder and Zhang 2003; Tong and Xue 2005; Xue et al. 2006; Jung et al. 2008a,b). In this study, rather than using the methods mentioned above, the Variational Doppler Radar Analysis System (VDRAS; Sun and Crook 1997), a radar data assimilation system based on the 4DVAR technique, is employed to perform all the numerical experiments, with the research goal focusing on the quantitative precipitation forecast (QPF).

It is known that the 4DVAR method requires an adjoint model, whose numerical scheme structures need to closely follow the prognostic model used for performing forward time integration. Greater complexity in the model development is expected if the terrain is to be resolved. The Japan Meteorological Agency (JMA) has established operational mesoscale models equipped with 4DVAR data assimilation capability (Saito et al. 2006). These systems use ≥ 10 -km spatial resolution, and are formulated in terrain-following coordinates. Significant improvements in terms of quantitative rainfall forecasts over the Japanese islands are achieved after assimilating observational data such as GPS precipitable water vapor or surface precipitation measurements (Nakamura et al. 2004; Koizumi et al. 2005).

The potential of VDRAS as a research platform for the short-term forecasting of severe storms in the American Great Plains has been demonstrated (Sun 2005; Sun and Zhang 2008). VDRAS was also implemented in operational mode to provide real-time wind and/or temperature fields for nowcasting purposes (Warner et al. 2007; Sun and Crook 2001; Crook and Sun 2002). It should be pointed out that since the forward cloud model in VDRAS is formulated within a Cartesian coordinate system with a flat surface, its performance over an area with complex terrain becomes an important issue. Warner et al. (2000) compared the rainfall estimates from Weather Surveillance Radar-1988 Doppler (WSR-88D), S-band dual-polarization Doppler radar (S-Pol) of the National Center for Atmospheric Research (NCAR), VDRAS simulations, and forecasts by an automated algorithm system, for prediction of a flash flood that occurred in complex terrain near Buffalo Creek, Colorado. They

concluded that although VDRAS did show considerable errors in the temporal variation of the rain rate, its precipitation simulations were generally superior to those obtained from the automated algorithmic system. A recent article by Sun et al. (2010) reported on the implementation of VDRAS during the Beijing 2008 Forecast Demonstration Project for the Beijing Summer Olympics. Their results showed that VDRAS could provide very useful information for nowcasting convective initiation, even though a substantial portion of the analysis domain was composed of complex terrain ranging in height from 300 to 2400 m.

This study presents the first attempt to apply VDRAS in Taiwan and vicinity. The topography of the island of Taiwan is complex. It has often been found that the steep mountains, with peaks reaching nearly 4000 m, can significantly enhance precipitation, or alter the rainfall distribution (Chien and Kuo 2006; Yang et al. 2008). The surrounding oceans (Taiwan Strait, Bashi Channel, and Pacific Ocean; see Fig. 2) also set a serious limitation on deploying in situ instruments. These factors pose great challenges to the running of VDRAS. Therefore, the primary purpose of this study is to find an appropriate strategy to apply VDRAS in this region.

In the next section the VDRAS system will be briefly introduced. Section 3 describes the first selected real case, intensive operation period (IOP) 8 from the Southwest Monsoon Experiment (SoWMEX). In section 4, the data sources, the preparation of the background fields, and the VDRAS model configuration are discussed. Several indices that are needed for verifying the VDRAS-predicted wind fields and precipitation are shown in section 5. The sensitivity of the VDRAS analysis and simulated fields to different background fields is investigated in section 6. Section 7 demonstrates the merit of merging VDRAS and the Weather Research and Forecasting Model (WRF) to improve the QPF accuracy. Section 8 shows the results of applying the same assimilation procedure to a second real case study, IOP 4 of SoWMEX, followed by a summary and future work in section 9.

2. The VDRAS radar data assimilation system

In VDRAS, a cloud-scale model formulated using the Cartesian coordinate system and a warm rain microphysical process, is adopted as a forward forecast model (Sun and Crook 1997). Using this prognostic model as a constraint and applying the 4DVAR technique, VDRAS is able to find an optimal initial state that minimizes a cost function (J), which measures the distances between the model predictions and the observations, and can be written as

$$J = (\mathbf{x}_o - \mathbf{x}_b)^T \mathbf{B}^{-1} (\mathbf{x}_o - \mathbf{x}_b) + \sum_{\sigma, t} [(\eta_v(v_r - v_r^o)^2 + \eta_q(q_r - q_r^o)^2)] + J_p + J_{mb}. \quad (1)$$

In (1), the summation is conducted over space (σ) and time (t), \mathbf{x}_o is the model state variables at the beginning of the current assimilation window, \mathbf{x}_b is the background field forecasted from the previous cycle, and \mathbf{B} symbolizes the background error covariance matrix. The coefficients η_v and η_q stand for the inverse of the observational error variance for radial wind and rainwater, respectively. The model-generated Doppler radial velocity and rainwater mixing ratio are represented by v_r and q_r , while their observed counterparts are expressed by v_r^o and q_r^o , respectively. Assuming a Marshall–Palmer raindrop size distribution, the rainwater mixing ratio (q_r in g kg^{-1}) can be estimated from the radar reflectivity by the following formula (Sun and Crook 1997):

$$q_r = \frac{1}{\rho} 10^{[(Z-43.1)/17.5]}, \quad (2)$$

where Z is the reflectivity in dBZ and ρ is the density of air. A penalty term (J_p) is applied in (1) to implement additional constraints such as temporal or spatial smoothing to the numerical solutions. Finally, the term J_{mb} denotes a mesoscale background field, whose impacts on the VDRAS solutions will be discussed later in this paper.

It should be pointed out that in VDRAS the forward model is a fully nonlinear model, instead of the tangent linear model as in the incremental formulation. The basic state in the adjoint is updated every iteration. VDRAS is composed of four major components, namely, data acquisition, preprocessing, data assimilation, and model outputs. The readers can refer to Sun and Zhang (2008) for a detailed description of VDRAS.

3. Description of case 1: SoWMEX IOP 8

The first real case selected for examination is from IOP 8 of SoWMEX. SoWMEX was conducted from May to June 2008, in the southwestern part of Taiwan. The scientific purposes of this experiment were to understand the kinematic and thermodynamic characteristics of the prevailing southwesterly flows, the physical processes leading to intensive orographic rainfalls, and the mechanisms that trigger heavy precipitation in the South China Sea and Taiwan during the Asian summer monsoon season. The primary application of knowledge on these issues is to improve the accuracy of the quantitative precipitation estimation (QPE) and forecasts (Lee et al. 2009).

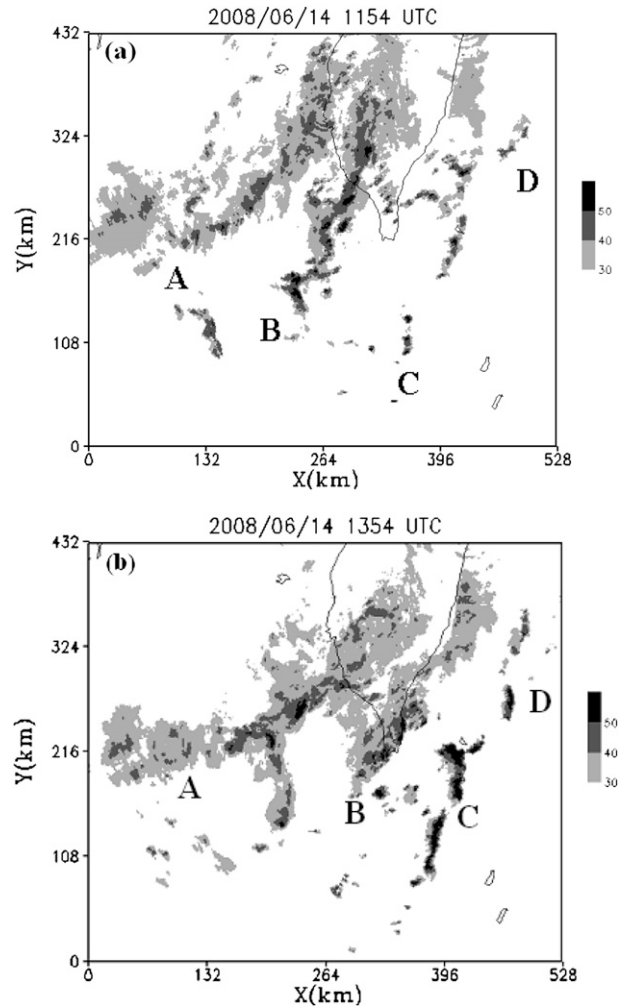


FIG. 1. Composite of the observed maximum radar reflectivity (dBZ) on 14 Jun 2008 for case 1 (IOP 8) at (a) 1154 and (b) 1354 UTC. The four major convection systems are labeled (A, B, C, and D).

The IOP 8 started at 0000 UTC 14 June and ended at 0000 UTC 16 June. According to the synoptic weather chart (not shown) at 1200 UTC 14 June, there was a low pressure center near Shanghai in China, and a frontal system was identified to the northwest of Taiwan. The low-level prevailing southwesterly winds were from the south of the Taiwan Strait and Bashi Channel. They brought warm and moist air from the oceans and produced heavy precipitation on the island. The 24-h accumulated rainfall for 14 June in the southwestern Taiwan area exceeded 100 mm. In some places the rainfall may have reached as high as 200 mm. Figure 1 illustrates the distributions of the composite maximum radar reflectivities at 1154 and 1354 UTC, observed by two Taiwan Central Weather Bureau (CWB) operational S-band Doppler radars (RCCG and RCKT; see Fig. 2 for their

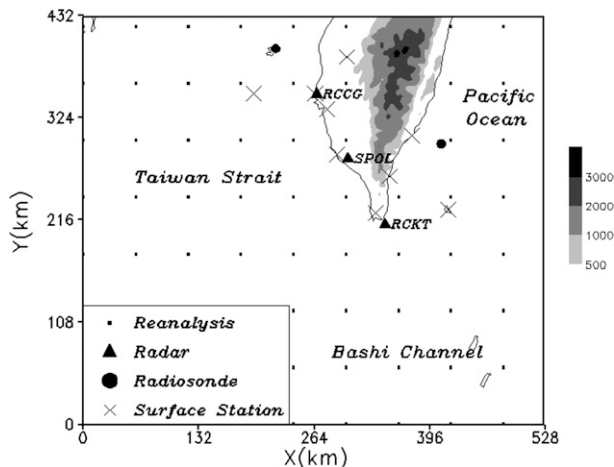


FIG. 2. The locations of data collected from different sources for case 1 (IOP 8). Triangles indicate radars, solid circles represent radiosondes, crosses stand for surface mesonet stations, and the small dots denote reanalysis data points from the NCEP–NCAR or ECMWF reanalyses. Two radiosondes released beyond the northern boundary of the domain are also used. This is also the simulation domain employed for the VDRAS model.

geographic locations). Four major convection systems, labeled A, B, C, and D, can be recognized. The magnitude of the reflectivity within these areas of convection reached above 50 dBZ. The first two systems, elongated in an NE–SW direction and moving toward the east and southeast, were responsible for heavy precipitation over southern Taiwan.

4. Data sources, mesoscale background field, and the VDRAS model setup for case 1 (IOP 8)

The data used for this study were collected from four radiosondes, nine surface mesonet stations, and two CWB Doppler radars (RCCG and RCKT). Although the NCAR S-Pol radar was also deployed in southern Taiwan during SoWMEX, its datasets were used only for verification. This is because the primary purpose of this research is to assess the performance of VDRAS using observations obtained within an operational framework. Figure 2 illustrates the locations of the instruments mentioned above. In addition, when preparing the background fields for some experiments, reanalysis data from the National Centers for Environmental Prediction (NCEP), or the European Centre for Medium-Range Weather Forecasts (ECMWF), were employed to fill in data-void regions over the oceans. Figure 2 also shows the topography of Taiwan. Starting from the plains along the western coastline, the terrain increases in height toward the mountains in the east, where peaks in the analysis domain can exceed 3500 m.

Continuous volume scans conducted by the RCCG and RCKT radars covered a maximum range of 230 km

under Doppler mode. Each volume scan took about 7.5 min, and contained nine elevation angles (0.5°, 1.4°, 2.4°, 3.4°, 4.3°, 6.0°, 9.9°, 14.6°, and 19.5°).

The background field consists of the horizontal wind, pressure, temperature, and water vapor mixing ratio. In this study, the background field is prepared by using the Barnes scheme to interpolate radiosonde and surface mesonet station observations to the model grid points. In some experiments, data from the NCEP–National Center for Atmospheric Research (NCAR) or ECMWF reanalyses are also adopted. These data, obtained from selected locations over the southern Taiwan Strait and Bashi Channel, have a relatively higher spatial resolution than the sounding and mesonet station data. Similar to the in situ measurements, the reanalysis data are also incorporated into the model grids by the Barnes technique. The interpolation can be expressed by

$$\phi_j = \frac{\sum_{i=1}^N W_i \phi_i^o}{\sum_{i=1}^N W_i} \quad \text{and} \quad (3)$$

$$W_i = e^{-(\Gamma r/R)^2}, \quad (4)$$

where ϕ_j is the interpolated value of variable ϕ at grid point j , ϕ_i^o is the observed ϕ at observational site i , W_i represents the weighting coefficient, r stands for the distance between the site and the grid point, R denotes the radius of influence, and Γ is used to control the amount of smoothing. When preparing the background field, R and Γ are set to 200 km and 0.66, respectively. Note that the procedure of successive correction is not used here. Thus, (3) is applied only once.

The VDRAS model for the IOP 8 case comprises a set of $264 \times 216 \times 30$ grid points, and the horizontal grid size (Δx and Δy) and vertical resolution (Δz) are 2.0 and 0.5 km, respectively. This is equivalent to a physical domain of $528 \times 432 \times 15 \text{ km}^3$. The simulation domain used by the VDRAS model is also shown in Fig. 2. A series of tests are first conducted to determine the number of assimilation windows. Since a sufficient amount of radar data is required in the assimilation, and it is also necessary to keep the computational cost affordable, our tests indicate that using three assimilation windows would be an appropriate choice. The assimilation strategy is depicted in Fig. 3. Basically, the entire data assimilation procedure starts at 1046 UTC 14 June 2008 and ends at 1154 UTC. During this period of time, three assimilation windows (1046–1101, 1109–1124, 1139–1154 UTC) are included. Each window lasts for approximately 15 min, and two model forecast periods are inserted in between. According

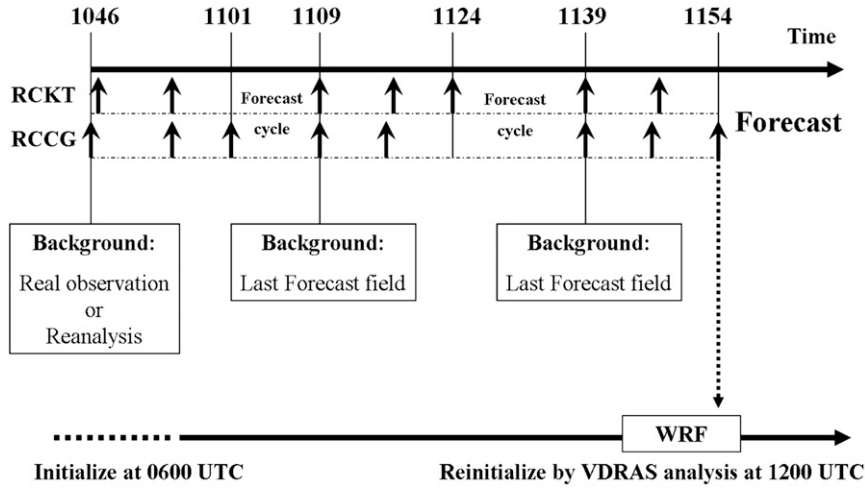


FIG. 3. VDRAS radar data assimilation design for case 1 (IOP 8). The numbers at the top of the diagram are the starting and finishing times (UTC) of each assimilation window. The upward-pointing arrows depict the input radar volume scan data collected by the radars listed on the left (RCKT and RCCG). The times at which WRF is initialized and merged with VDRAS are shown at the bottom of the diagram.

to Sun and Zhang (2008), implementing such a forecast period between the assimilation windows can significantly improve the accuracy of the VDRAS retrievals. Radar data observed by RCCG and RCKT, but from a different number of volume scans, are assimilated into VDRAS. The entire assimilation process is completed at 1154 UTC, followed by a 2-h model forecast. The retrieved analysis fields and the QPF capability of VDRAS for this case study will be examined in the following sections.

5. Indices for quantitative verification of rainfall and wind forecasts

To verify the rainfall amount forecasted by VDRAS, we first compute the instantaneous rain rate R at each grid point on the lowest model layer (i.e., 0.25 km) as follows:

$$R = \frac{q_r V_T \rho_a}{\rho_w}, \quad (5)$$

where q_r (kg kg^{-1}) is the rainwater mixing ratio; ρ_a and ρ_w (kg m^{-3}) represent the air and water densities, respectively; and V_T (m s^{-1}) stands for the terminal velocity. According to Sun and Crook (2001), V_T can be estimated from the radar reflectivity Z (in dBZ)

$$V_T = 5.4 \times 10^{0.00714(Z-43.1)}. \quad (6)$$

Since R has the units meters per second, it is converted to the rainfall amount (mm) for each model time step (ΔT) by

$$\text{PRE} = R \times 1000 \times \Delta T. \quad (7)$$

The parameter PRE in (7) is accumulated for 2 h, then compared against the measurements from 166 rain gauges, whose locations are shown in Fig. 4.

For the purposes of comparison, the VDRAS-predicted rainfall amounts distributed at the model grid points are interpolated to each rain gauge site. Here, the interpolation is also performed using a Barnes scheme, as expressed by (3) and (4), but the radius of influence R is 10 km, and Γ is given a value of 1.0. The equitable threat score (ETS), as proposed by Schaefer (1990) and Rogers et al. (1996), is computed to provide a quantitative comparison of the QPF accuracy under different scenarios. This index is defined as

$$\text{ETS} = \frac{H - R}{F + O - H - R}, \quad (8)$$

where H is the number of correctly predicted points above a certain threshold, F stands for the number of forecast points above a threshold, O represents the number of observed points above a threshold, and R is the number of hits by chance, which can be written as

$$R = \frac{F \times O}{N}, \quad (9)$$

where N is the total number of points in the verification domain. The ETS is designed to evaluate the forecast capability beyond a random guess. If H is the same as R , then the ETS shows a forecast skill score of zero; whereas $\text{ETS} = 1$ implies a perfect forecast.

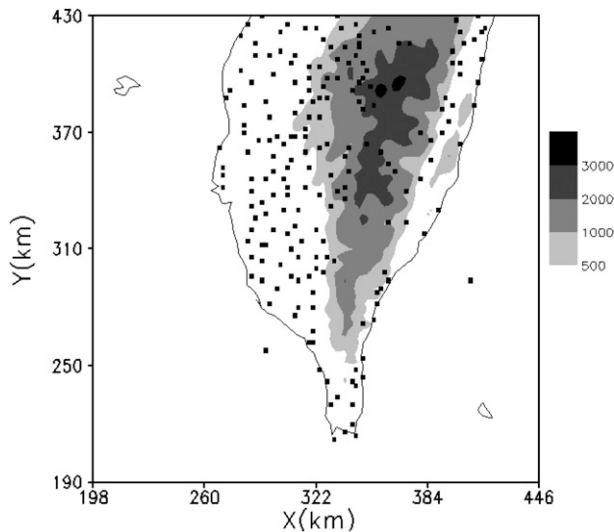


FIG. 4. Distribution of 166 rain gauges used for QPF verification. The terrain (m) is represented by shading at 500- and 1000-m intervals.

Other indices utilized when conducting a quantitative comparison between the simulated and observed variables include the root-mean-square error (RMSE) and the spatial correlation coefficient (SCC):

$$\text{RMSE} = \sqrt{\frac{\sum (A_P - A_O)^2}{M}} \quad \text{and} \quad (10)$$

$$\text{SCC} = \frac{\sum (A_P - \bar{A}_P)(A_O - \bar{A}_O)}{\sqrt{\sum (A_P - \bar{A}_P)^2 \sum (A_O - \bar{A}_O)^2}}. \quad (11)$$

In (10) and (11), subscripts P and O denote the VDRAS-predicted and observed values for a certain parameter A , respectively, and M stands for the total number of grid points used for the calculation. In (11) the overbars denote an area average over either a two-dimensional plane or a three-dimensional space.

6. Sensitivity to the background fields

a. VDRAS analysis fields

In this set of experiments the background fields prepared from different data sources are tested to study their impacts on the VDRAS-retrieved analysis fields and rainfall forecasts. In experiment OBS, the background field is constructed by using the Barnes method to interpolate observational data from only four radiosondes and nine surface mesonet stations to the model grid points. In the experiments named NCEP and EC, the NCEP–NCAR or ECMWF reanalysis data obtained

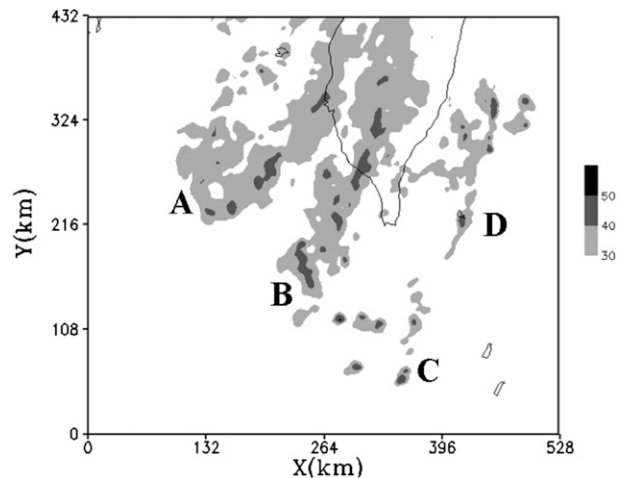


FIG. 5. VDRAS-retrieved maximum radar reflectivity field for case 1 (IOP 8) at 1154 UTC from experiment OBS_EC.

at locations inside the computational domain (see Fig. 2) are also interpolated to the model grid points using the Barnes method. Finally, in experiment OBS_EC, the background field is obtained by combining both the in situ and ECMWF reanalysis datasets.

Although differences do exist in the magnitudes and detailed spatial structures, the major kinematic and thermodynamic characteristics retrieved by VDRAS turn out to be quite similar for the four different types of background fields. Thus, only experiment OBS_EC is selected as an example to further study the fine structures within the precipitation systems. Figure 5 displays the retrieved maximum radar reflectivity fields at 1154 UTC from experiment OBS_EC. The result is generally in good agreement with the observations (see Fig. 1a). The four observed convection systems (A, B, C, and D) are all successfully reconstructed. However, convection system A appears to have a shorter extension toward the west than that shown by the radar echoes at $x < 132$ km, as illustrated in Fig. 1a. This is due to the fact that the radar reflectivity in that region is detected by low-elevation-angle scans in non-Doppler mode with a low pulse repetition frequency. The Doppler radial winds are actually not available in that area. As a result, only the radar data at $x > 132$ km are assimilated into VDRAS.

A comparison of the wind and convergence fields (not shown) before and after assimilation of the radar data reveals that before the radar data are assimilated, the analysis domain contains information only from the synoptic-scale environmental field. However, after assimilating the radar data, the convergence field produced by VDRAS begins to exhibit more detailed small-scale features. The magnitude also increases by nearly $10\text{--}10^2$ times.

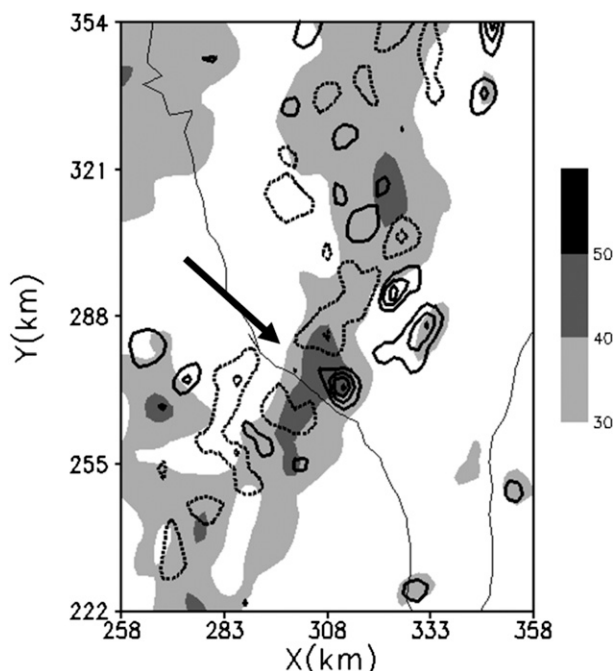


FIG. 6. Radar reflectivity (shading with 10-dBZ intervals) and vertical velocity (contours with 0.3 m s^{-1} intervals) at $Z = 1.25 \text{ km}$ in convection system B retrieved in experiment OBS_EC at 1154 UTC for case 1 (IOP 8). Updrafts (downdrafts) are depicted by solid (dashed) lines. The maximum updraft can reach 2.0 m s^{-1} . The thick solid arrow indicates the direction of the movement. The thin line is the coastline of southern Taiwan.

A closer assessment of convection line B is also conducted to demonstrate the reliability of VDRAS. Figure 6 shows the retrieved radar reflectivity and vertical velocity of system B at $Z = 1.25 \text{ km}$, while Fig. 7 displays the horizontal wind vectors and convergence field at a lower altitude with $Z = 0.25 \text{ km}$. It can be seen that regions with strong reflectivity are generally associated with low-level convergence. The updraft maxima are analyzed near some strong reflectivity areas and on the mountain slope. The maximum upward motion can reach 2.0 m s^{-1} . In the direction of motion (southeast), upward motion and a low-level convergence field can be found on the front portion of the convection line (see $x \approx 308 \text{ km}$, $y \approx 272 \text{ km}$ in Fig. 6). The convergence at the leading edge can trigger the development of new cells, so that the convection line continues to move toward the southeast. It is also interesting to note (see Fig. 7) that there is a narrow elongated band of convergence along the local topography that can be clearly identified near $x \approx 333 \text{ km}$ and $240 \text{ km} < y < 288 \text{ km}$. This convergence is believed to be induced due to the blockage of the southwest flows by the mountains. This indicates that although VDRAS is formulated over a flat surface, the retrieved kinematic field still reflects the influence imposed by the terrain.

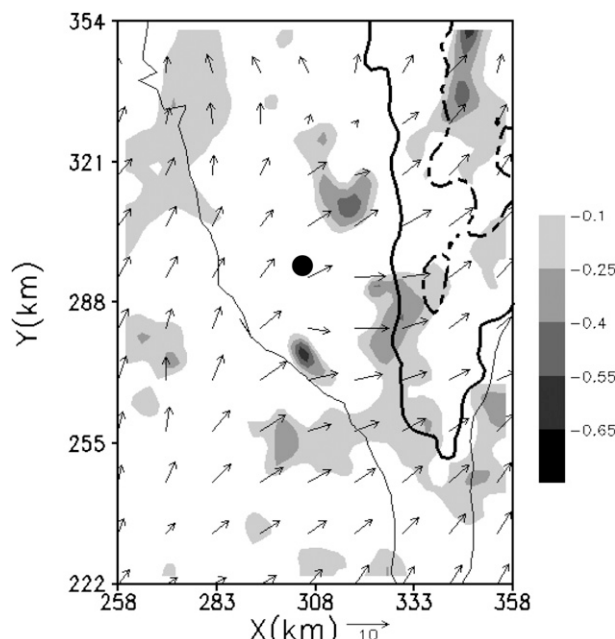


FIG. 7. As in Fig. 6, but for the horizontal convergence field and wind vectors at $Z = 0.25 \text{ km}$. For simplicity, only convergence is plotted. The magnitude has been amplified 10^3 times. The thick solid and dashed lines denote the terrain at heights of 500 and 1500 m, respectively. The solid circle depicts the location of the Pingdong sounding station.

Since information of the deceleration about the southwest flow is embedded in the observed Doppler radial winds, the topographic effects of the mountains can still be revealed by VDRAS through 4DVAR assimilation of the radar data.

To verify the accuracy of the analyzed wind field, Fig. 8 shows a comparison of the winds generated by VDARS at 1154 UTC, and those measured at 1200 UTC by a sounding released at the Pingdong station (see Fig. 7 for the location). Note that since the Pingdong sounding data are not used for the entire assimilation procedure, they can be considered to be independent data for verification. Figure 8 illustrates the consistency of vertical structures from both model and sounding results, especially below 5.0 km. The larger discrepancies that occurred in the upper layers can be attributed to the drift of the sounding from the Pingdong station. The RMSEs of the u and v winds are 2.96 and 3.82 m s^{-1} , respectively. These errors are comparable to the values reported by Sun et al. (2010).

Figure 9 shows the retrieved temperature perturbations (calculated by subtracting a horizontal mean) at the 0.25-km height. It is evident that the low-level cold pool behind the leading edge, with the minimum temperature perturbation reaching -1.0°C , is recovered. To verify whether the magnitude of the model-produced cold pool is reasonable, the VDRAS outputs are again

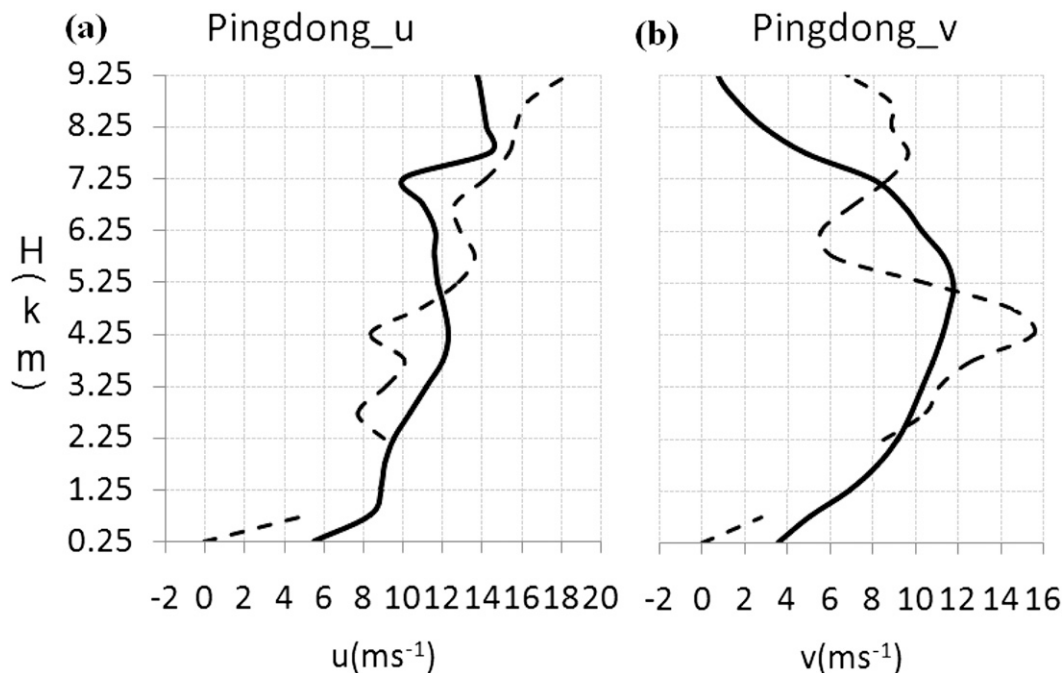


FIG. 8. VDRAS-produced (solid) and sounding-observed (dashed) wind components: (a) u and (b) v at the Pingdong station for case 1 (IOP 8).

compared against the temperature measurements from the Pingdong sounding, which is located inside the cold pool region, as depicted in Fig. 9. Furthermore, the temperature profile from the Green Island sounding is also adopted for comparison. It can be seen in Fig. 9 that Green Island is in the warmer region. However, it should be mentioned that the temperature data from the Green Island sounding are applied when preparing the background field. As shown later, this leads to a smaller difference between the VDRAS simulation and sounding observations from the Green Island site. This can be considered to be an indication that the information about the temperature at this location has been assimilated into the model.

The results of our comparison are shown in Fig. 10. The VDRAS temperature profiles are generally consistent with the sounding observations. The RMSEs for the temperature between the sounding measurement and the VDRAS simulation at Pingdong and Green Island are 1.22°C and 0.43°C , respectively. The temperature measured at the Green Island station is indeed higher than that measured at the Pingdong station. The observed temperature deficit at $Z = 0.25$ km between Pingdong and Green Island reaches -2.6°C . The VDRAS-simulated temperature distribution also exhibits a similar spatial trend, but with a smaller temperature difference of about -1.3°C . Since the VDRAS analysis field is produced through fitting the model's numerical solutions to the observations, this discrepancy is believed to be caused

by the smoothing of the model (Sun et al. 2010). Overall, the aforementioned description suggests that VDRAS is able to produce reasonable small-scale kinematic and thermodynamic features after the assimilation of Doppler radar data.

b. VDRAS model predictions: Radar reflectivity

The discussion in the previous section shows that VDRAS is able to recover reliable analysis fields using the 4DVAR technique. However, its performance in predicting severe convective systems in Taiwan, especially rainfall forecasts, needs to be examined carefully. This is because the steep terrain that characterizes the island is expected to complicate the interaction between the airflow and the land. However, the forward model in VDRAS is not formulated in a terrain-following coordinate. Moreover, the surrounding ocean imposes a serious limitation on the deployment of in situ instruments. These factors become challenging issues when we attempt to apply VDRAS in the Taiwan area.

An optimal initial model state is obtained at 1154 UTC after the assimilation of the Doppler radar data is completed. VDRAS continues with the integration for two more hours. The simulation results based on different background fields are discussed in this section.

The predicted maximum radar reflectivities at 1354 UTC from experiments OBS, NCEP, EC, and OBS_EC are plotted in Fig. 11. Compared with the observations

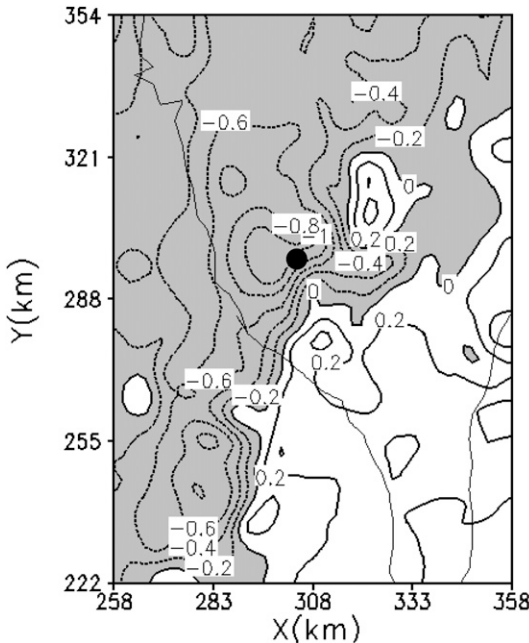


FIG. 9. VDRAS temperature perturbations at $Z = 0.25$ km for case 1 (IOP 8). The solid (dashed) lines denote positive (negative) perturbations, at an interval of 0.2° . The region with negative values is shaded. The Pingdong and Green Island (outside the domain) sounding stations are represented by a circle and a triangle, respectively.

(Fig. 1b), the predicted convection system A for all four experiments tends to develop to a greater intensity than in the observations, and spreads over a broader area toward the north and south. Its westward extension to the southern Taiwan Strait is further constrained as time passes. The portion over the island has shifted farther north than the observations after 2 h of simulation time. However, for convection system B for all four experiments, VDRAS accurately captures its movement toward the southern tip of the island during the following 2-h period. We believe that this is because convection system B is better monitored by radar scans than are the other systems. In contrast, it is indicated in Fig. 11a that experiment OBS fails to predict the evolution of convection C located over the Bashi Channel at 1354 UTC. It should be pointed out that in OBS, the background environment is provided by interpolating only the ground-based in situ measurements to the entire analysis domain. Consequently, the interpolated background field over the Bashi Channel could become rather unrealistic due to its great distance from the land. To further illustrate this issue, experiments NCEP and EC are designed to utilize NCEP–NCAR or ECMWF reanalysis data for the background fields. The resulting simulated reflectivity fields shown in Figs. 11b and 11c illustrate that convection system C is indeed better simulated by VDRAS after 2 h

of model integration, although its intensity and extent are substantially overpredicted in experiment NCEP. An additional examination of the low-level moisture field (not shown) reveals that the background environment of experiment OBS over the Bashi Channel is much drier than that of experiments NCEP and EC. This may explain why convection system C has difficulty developing in experiment OBS. Since the predicted radar reflectivity and rainfall (to be discussed in the next section) from experiment EC turn out to be better than those from experiment NCEP, we decide to combine soundings, surface stations, and ECMWF reanalysis data to reconstruct a new background field. The simulation based on this background field is called experiment OBS_EC. As expected, convection systems A and B over land, and convection system C over the ocean, are still maintained in OBS_EC, as can be seen in Fig. 11d. However, convection system C grows into scattered cells, rather than a convection line, as detected by the radar observations shown in Fig. 1b. Finally, the VDRAS-produced area of convection system D that appears over the Pacific Ocean in all four experiments also evolves into a stronger and wider system than is seen in the observations. This would cause an overestimation of the rainfall amount in eastern Taiwan.

c. VDRAS model predictions: Wind and QPF skill

To assess the accuracy of the winds, the model-predicted three-dimensional winds are first projected to NCAR S-Pol (see Fig. 2 for its location). They are then compared against the Doppler radial velocities measured by S-Pol. The projection is processed utilizing the following formulas:

$$V_r = \frac{(x - P_x)}{r}u + \frac{(y - P_y)}{r}v + \frac{(z - P_z)}{r}w + V_T \quad (12)$$

and

$$r = \sqrt{(x - P_x)^2 + (y - P_y)^2 + (z - P_z)^2}. \quad (13)$$

In (12) and (13), (u, v, w) is the three-dimensional wind and V_r is the projected radar radial wind. The coordinates of the grid point and the S-Pol radar are represented by (x, y, z) and (P_x, P_y, P_z) , respectively, while the distance between them is denoted by r . The terminal velocity (V_T) can be estimated by the simulated radar reflectivity using (6). Note that the curvature of the earth is neglected in (12) and (13). Its influence on determining the locations of radar measurements is discussed in Brewster (2003) and Gao et al. (2006). The RMSEs of the projected and observed radial winds are evaluated using (10), and are adopted as a quantitative index to describe the accuracy of the VDRAS-simulated flow field. Since the Doppler

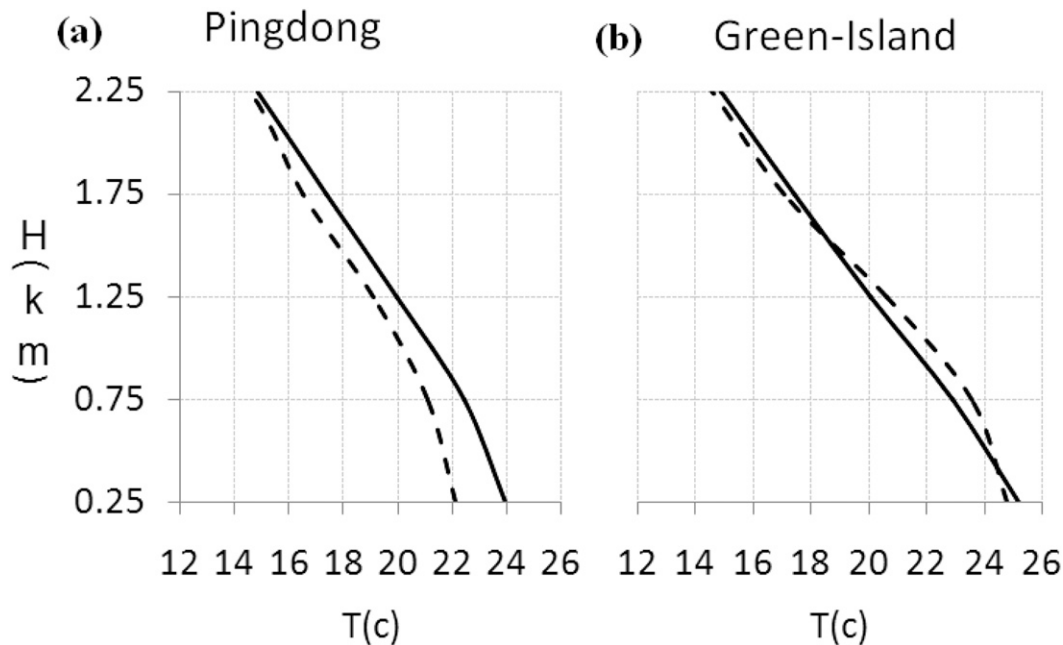


FIG. 10. VDRAS-simulated (solid) and sounding-observed (dashed) total temperature profiles at the (a) Pingdong and (b) Green Island stations for case 1 (IOP 8).

wind data are taken from volume scans, the comparison with S-Pol radial velocity fields should be considered to be a three-dimensional verification.

Figure 12 displays the root-mean-square error over the entire observation volume during the 2 h of model integration between the VDRAS-forecast radial winds and their observed counterparts in experiments OBS, NCEP, EC, and OBS_EC. It can be seen that the error increases with time for all four experiments, but remains below 5.0 m s^{-1} . The flow structure is better described in experiment OBS_EC than in OBS, NCEP, and EC, as indicated by its having the smallest RMSEs ($<3.5 \text{ m s}^{-1}$) during the entire model simulation period. The significant reduction of error in OBS and OBS_EC from NCEP and EC also suggests the importance of using updated observations from radiosonde and surface stations in the background field.

Figure 13 shows a comparison of the ETSs, defined in section 5, of the predicted 2-h accumulated rainfall amounts at different precipitation thresholds [6, 10, 14, and 18 mm (2 h)^{-1}] obtained in the four experiments. It is found that experiment OBS produces better rainfall forecast at a lower threshold [6 mm (2 h)^{-1}]. The rainfall forecasts for experiment NCEP are poor, with ETS scores below 0.1 for all thresholds. Experiment OBS_EC performs considerably better for heavy rainfall events [e.g., 14 and 18 mm (2 h)^{-1}]. The ETS from experiment EC is generally lower than the one produced by either OBS or OBS_EC, or both.

The RMSE and SCC of the forecasted precipitation are listed in Table 1. Experiment NCEP turns out to have the lowest SCC (0.13) and highest RMSE (13.1 mm) among the four experiments. Experiment OBS_EC produces better results (higher SCC and lower RMSE) than experiment EC, which indicates the importance of adding in-site observations to the background fields. Experiments OBS_EC and OBS seem to perform comparably well in forecasting the rainfall amount, since OBS_EC has a higher SCC, but OBS has a lower RMSE. However, recall that in experiment OBS, convection system C over the Bashi Channel completely disappears after 2 h of simulation, as opposed to what occurs in OBS_EC (see Figs. 11a and 11d). Moreover, as mentioned earlier, OBS_EC is persistently superior in simulating the velocity field. Thus, it can be concluded that a synergy of the ground-based in situ observations and the ECMWF reanalysis data over the oceans, as is found in OBS_EC, would be a more appropriate strategy for preparing the background field than using either one of the data sources alone.

Figure 13 demonstrates that the ETSs produced by OBS_EC are generally between 0.1 and 0.2. It would be interesting to compare our results with other studies where QPF skills for mesoscale phenomena are discussed. However, one should keep in mind that these studies may differ substantially in many aspects. Xiao et al. (2005) applied the 3DVAR method to assimilate Doppler radar data collected in the Korean Peninsula. They reported that for the first 6-h forecast, the best

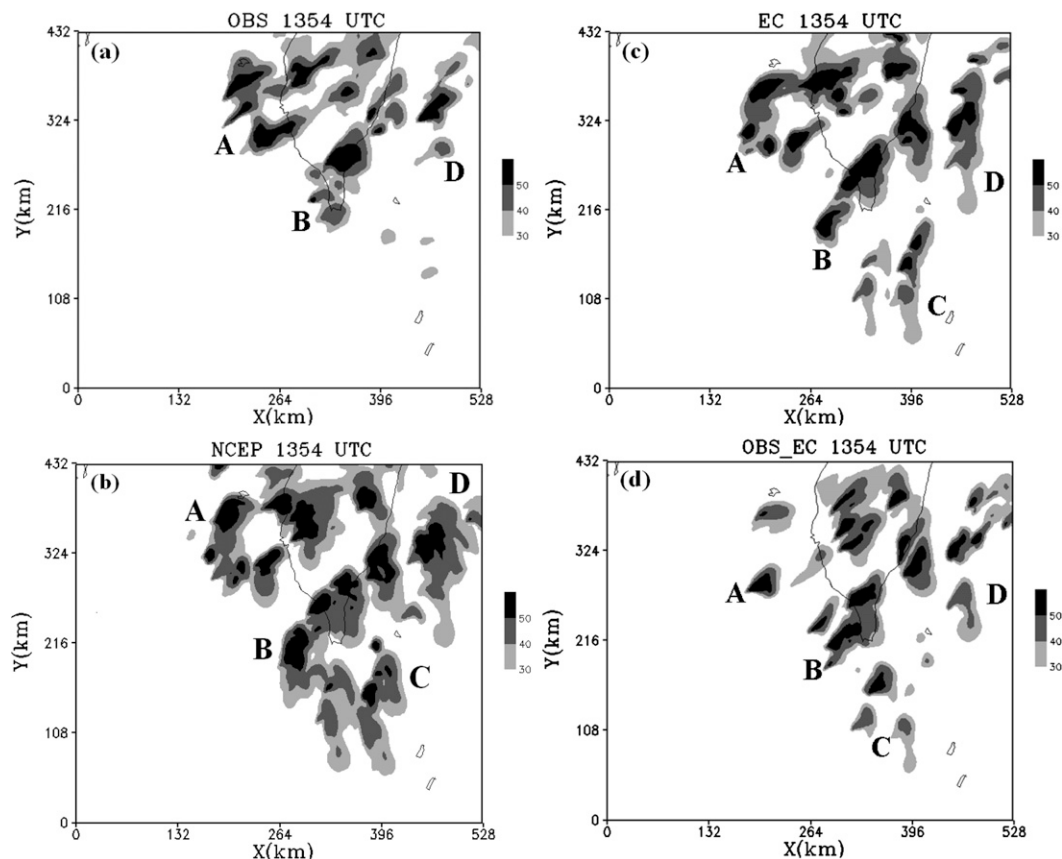


FIG. 11. VDRAS-predicted maximum radar reflectivity fields for case 1 (IOP 8) at 1354 UTC from experiments (a) OBS, (b) NCEP, (c) EC, and (d) OBS_EC. They represent the 2-h forecasts after the assimilation procedure is completed at 1154 UTC.

threat scores for the 3-h accumulated rainfall were approximately 0.38 and 0.25 at 5- and 10-mm thresholds, respectively. It should be pointed out that the threat score index used in their calculation tends to overestimate the forecast skill, since it is a biased score that also depends upon the frequency of the event that is forecasted (Schaefer 1990). Sun and Zhang (2008) utilized VDRAS and multiple Doppler radars to study a squall line observed in the United States during the IHOP experiment. The threat score for the predicted 5-h accumulated rainfall from their experiments could reach 0.5 in the case of light rain [$2.0 \text{ mm (5 h)}^{-1}$]. This value drops rapidly to less than 0.1 when the amount of precipitation increases beyond $14.0 \text{ mm (5 h)}^{-1}$. Clark et al. (2009) compared rainfall forecast skills over the central United States obtained from a 5-member, 4-km spatial-resolution and a 15-member, 20-km spatial-resolution WRF ensemble. The average ETSS, under different thresholds (0.10, 0.25, and 0.50 in.), and for 1-, 3-, and 6-hourly accumulation intervals, were generally below 0.40. Similar QPF skill was also reported by Kong et al. (2009) using a real-time storm-scale ensemble forecast system, which

incorporated the Advanced Research WRF (ARW) core, the Nonhydrostatic Mesoscale Model WRF (WRF-NMM) dynamic core, and the Advanced Regional Prediction System (ARPS). Kain et al. (2010) evaluated the impacts of assimilating radar data and other mesoscale observations into a convection-allowing model during the

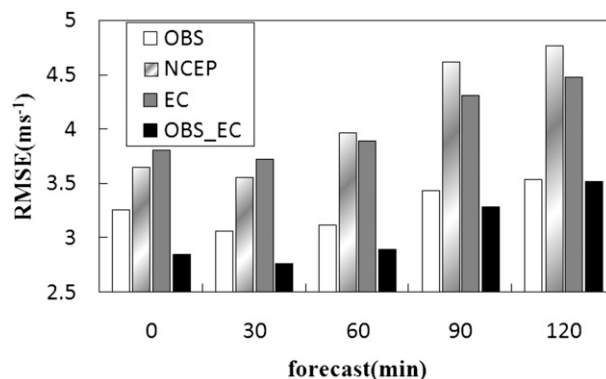


FIG. 12. Temporal variation of the RMSE (m s^{-1}) between the S-Pol-observed radial wind and the VDRAS-simulated radial wind in experiments OBS, NCEP, EC, and OBS_EC for case 1 (IOP 8).

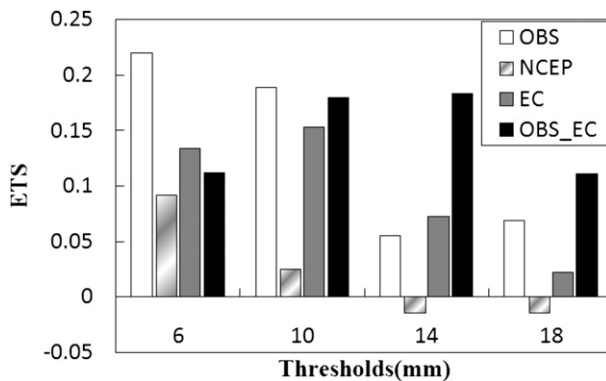


FIG. 13. ETSs for case 1 (IOP 8) from experiments OBS, NCEP, EC, and OBS_EC for the predicted 2-h accumulated rainfall amount at different precipitation thresholds.

spring seasons of 2008 and 2009 over the United States. Their study revealed that the positive effects of the assimilation were greatest during the first 3–6 h of the forecast. The ETS score, with the 1 mm h^{-1} threshold, ranged from 0.20 to 0.35 during this period of time.

Relevant research focusing on the Taiwan area can be found in Chien et al. (2002), in which they evaluated the QPF skill in this region utilizing the fifth-generation Pennsylvania State University–NCAR Mesoscale Model (MM5), with a 15-km model grid size. They computed the ETS for 12-h accumulated rainfall prediction, and found the highest score was 0.2 for the 2.5-mm criterion. Hong (2003) also used the 5-km-resolution MM5 to conduct rainfall prediction experiments for Taiwan and nearby regions. His results indicated that the ETS indices for the 12–24-h forecast were about 0.09–0.23 at different thresholds. The first 0–12 h turned out to have the poorest accuracy, with ETSs ranging from 0.22 to 0.03. Yang et al. (2004) proposed an ensemble-type forecast using the so-called multiple linear regression technique. In their experiments the ETSs for a 12-h period were from about 0.1 to 0.3 for light and medium rainfalls. Overall, the ETS values produced from our experiments are generally comparable to those obtained in earlier studies. Nevertheless, we attempt in this research to further improve the VDRAS forecast skill by merging it with the WRF, as discussed in the following section.

7. Merging VDRAS with WRF

Although VDRAS is formulated in a Cartesian coordinate with a flat surface, our experimental results indicate that its analysis fields can still reflect the influence of the topographic effects. However, if VDRAS is to be used for forecasting, especially in an area like Taiwan with its complex terrain, then this issue needs to be considered. In this investigation, it is proposed that the VDRAS analysis

TABLE 1. SCCs and RMSEs of forecasted 2-h accumulated precipitation.

	OBS	NCEP	EC	OBS_EC	OBS_EC+WRF
SCC	0.38	0.13	0.29	0.43	0.68
RMSE (mm)	8.5	13.1	10.2	9.0	5.8

fields be merged with the WRF, so that one can take advantage of WRF's terrain-resolving capability to better simulate the interaction between the convective systems and the mountains.

a. Method for merging the two models

The configuration of WRF consists of two domains (d01 and d02, as shown in Fig. 14). Both domains include 264×216 grid points in the horizontal and 46 σ layers in the vertical. The grid spaces are specified to be 6 and 2 km for d01 and d02, respectively. The pressure at the model top is 50 hPa. Two-way interaction is allowed between d01 and d02. The d02 grid system overlaps the VDRAS analysis domain to avoid additional interpolation. However, since VDRAS and WRF adopt different coordinate systems in the vertical direction, the geopotential height is used as a reference to interpolate the VDRAS analysis fields to the WRF vertical grids.

To merge the VDRAS analysis field with WRF without causing inconsistencies near the boundaries, the following formula is employed to determine the weighting coefficient for the WRF field. Letting D (km) be the distance from one of the radars, we have

$$W = \begin{cases} 0.0 & D < 100 \text{ km} \\ (D - 100) \times 0.01 & \text{for } 100 \text{ km} < D < 200 \text{ km} \\ 1.0 & D > 200 \text{ km} \end{cases} \quad (14)$$

The criteria for the distances used in (14) are obtained on a trial-and-error basis. They are selected so that the variables can transit smoothly from the VDRAS domain to the WRF domain. If W_{CG} and W_{KT} denote the weighting coefficients calculated for RCCG and RCKT, respectively, then their minimum would be applied for the interpolation at each grid point. That is

$$A' = A_{VDRAS} \times (1.0 - \alpha) + A_{WRF} \times \alpha \quad \text{and} \quad (15)$$

$$\alpha = \min(W_{CG}, W_{KT}), \quad (16)$$

where A_{VDRAS} and A_{WRF} represent a common parameter A simulated by VDRAS and WRF, respectively, while A' is the final interpolated value. The spatial distribution of α can be found in Fig. 15.

It should be pointed out that in VDRAS, the Kessler warm rain scheme (Kessler 1969) is employed, but in our

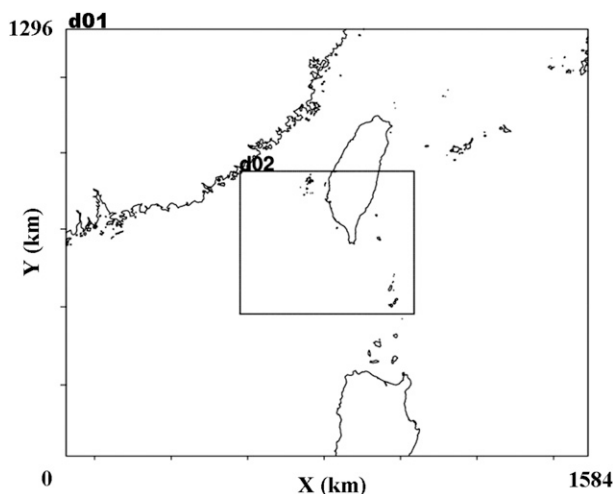


FIG. 14. Model domain configuration for the WRF system in case 1 (IOP 8). Domain d02 covers the same area as VDRAS.

WRF simulation, the scheme proposed by Lin et al. (1983) is used. As a result, only the parameters available in VDRAS are merged with WRF. These parameters include the three-dimensional wind (u , v , w), potential temperature perturbation (θ'), and water vapor (q_v), cloud water (q_c), and rainwater (q_r). Other microphysical variables that are available only in WRF, such as ice (q_i), snow (q_s), and graupel (q_g), are set to zero during the merging procedure. Finally, when the VDRAS results are merged with WRF, only those variables located above the terrain are utilized.

As described in section 6, pure VDRAS simulations are obtained based on four different background fields. On the other hand, WRF can be initialized using either NCEP–NCAR or ECMWF reanalysis data. Consequently, when merging VDRAS with WRF, there are eight different combinations. After taking into account two pure WRF runs without merging with VDRAS, a total of 10 tests are performed in this group of experiments, as listed in Table 2. However, for brevity, only test 8, the combination that produces the most accurate rainfall forecasts, is presented in this section. In test 8, also named experiment OBS_EC+WRF, the WRF is initialized at 0600 UTC using the ECMWF reanalysis field. It then starts the time integration for 6 h. At 1200 UTC, the VDRAS analysis fields obtained from experiment OBS_EC, as discussed in section 6, are merged with WRF. WRF is then allowed to run for another 2 h until 1400 UTC (see Fig. 3). For the purpose of comparison, test 10 (see Table 2) represents a pure WRF simulation in which WRF is initialized using ECMWF data at 0600 UTC. The simulation then runs until 1400 UTC without being combined with any of the VDRAS-produced fields. This is called experiment WRF. The results from these two experiments are also compared

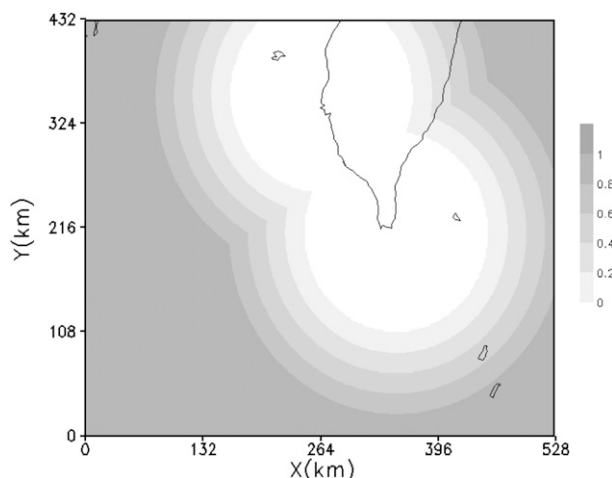


FIG. 15. Spatial distribution of the weighting coefficient α , defined by (14)–(16) in the text.

against those from experiment OBS_EC, which stands for an experiment using VDRAS alone.

b. Results

Figure 16 displays the ETSS of the forecasted 2-h accumulated rainfall from experiments OBS_EC, WRF, and OBS_EC+WRF. It can be clearly seen that at most of the precipitation thresholds, OBS_EC+WRF outperforms the other two experimental designs by a large margin. At the 6-, 10-, and 14-mm thresholds, the ETSS of experiment OBS_EC+WRF can reach 0.414, 0.393, and 0.230, as opposed to, respectively, 0.112, 0.179, and 0.183 from OBS_EC. The QPF skill obtained using WRF alone without VDRAS (i.e., experiment WRF) turns out to be rather poor, as revealed by the small ETSS in Fig. 16.

As shown in Table 1, the SCC and RMSE for experiment OBS_EC are 0.43 and 9.0 mm, respectively. It is found that in experiment OBS_EC+WRF, the SCC can be increased to 0.68, while the RMSE can be reduced to 5.8 mm. The aforementioned statistics indicate a significant improvement in QPF capability when VDRAS is combined with WRF.

Figure 17 shows the spatial distribution of the 2-h accumulated rainfall from rain gauge observations, and the predictions of all three experiments. The topographic effects are evident in Fig. 17a. The major precipitation is found to be concentrated along the western slopes of the mountains, with the maxima [$35\text{--}45\text{ mm (2 h)}^{-1}$] occurring slightly to the west of the peak, and at the southern tip of the mountains. In contrast, the eastern side of the mountains received relatively less rainfall [$<10\text{ mm (2 h)}^{-1}$]. It is exhibited in Fig. 17b that in experiment OBS_EC, the contours below 25 mm generally agree well with the observations. The heavy rainfall near the

TABLE 2. The experimental designs for merging VDRAS and WRF. WRF is initialized by utilizing NCEP–NCAR or ECMWF reanalysis data. The background field for VDRAS is prepared in four different ways, as described in section 6 of the text. Tests 9 and 10 denote two pure WRF runs without merging with VDRAS.

Test index	Initialization of WRF		Background field for VDRAS			
	NCEP	ECMWF	OBS	NCEP	EC	OBS_EC
1	X		X			
2	X			X		
3	X				X	
4	X					X
5		X	X			
6		X		X		
7		X			X	
8		X				X
9	X					
10		X				

southern tip of the mountains is well forecasted. However, there is an overprediction of heavy rainfall over the southwestern plain, over the mountain peak, and along the Pacific Ocean coastline in southeastern Taiwan. This is not surprising, since in this experiment the forecast is made by VDRAS only, in which the terrain is not resolved. Thus, in this experiment, topographic effects due to the mountains are not considered in the simulated airflow. Figure 17c reveals that since WRF is capable of coping with terrain variations, it does accurately forecast the small amount of rainfall along the eastern coastline. However, the pattern of accumulated rainfall on the western side of the mountains does not agree with the observations. Furthermore, a spurious heavy precipitation center is wrongly forecasted by WRF in the northwestern part of the domain. The heavy rainfall near the southern tip of the mountains is also completely missing. Finally, experiment OBS_EC+WRF offers the best match between the predicted rainfall and the observations both qualitatively and quantitatively, as shown in Fig. 17d. It successfully forecasts the two major precipitation bands over the southwestern plain and southern tip of the island, and the slight amount of rainfall in the southeastern coastal area. This success can be attributed to the assimilation of meso- and convective-scale information, detected by the Doppler radars, into VDRAS, and to the better treatment of the topographic effects during the WRF simulation.

8. Application to case 2: SoWMEX IOP 4

To further validate the proposed assimilation procedure introduced in the previous sections, the same experimental design as in test 8 (see Table 2), which produces the best rainfall forecast, is applied to a second case observed during IOP 4 of SoWMEX. This IOP started at 2100 UTC

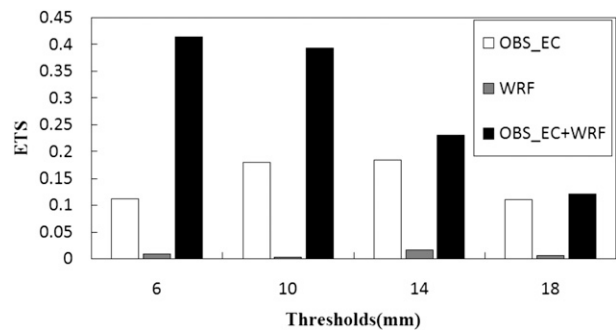


FIG. 16. ETSs of the forecasted 2-h accumulated rainfall for case 1 (IOP 8) from experiments OBS_EC, WRF, and OBS_EC+WRF, representing simulations using VDRAS only, WRF only, and a combination of both, respectively.

1 June and ended at 1500 UTC 3 June. The synoptic weather chart (not shown) at 0000 UTC 2 June revealed that a stationary front was identified stretching from south of Japan to the coast of southern China, and crossing southern Taiwan. Several line convections formed over the ocean. They began to interact with the topography as they approached the landmass of Taiwan. The observed 24-h accumulated precipitation for 2 June in the southwestern part of Taiwan exceeded 100 mm. A region with maximum rainfall reaching 200 mm day⁻¹ can be found near central Taiwan.

Our assimilation experiment covers a period of 3 h, starting from 0501 UTC 2 June. The model nested configuration and spatial resolutions are the same as in case 1 (IOP 8), except that d01 and d02 contain 258 × 276 grid points in the horizontal direction, which allows d02 to extend farther north and south. The entire assimilation algorithm lasts for 1 h from 0501 to 0601 UTC, and is composed of three 15-min assimilation windows, with two 7–8-min forecast periods in between. Similar to case 1, the background fields are also prepared using in situ measurements taken from six radiosondes and 12 surface stations on land, and the ECMWF reanalysis data over the ocean. The VDRAS analysis fields at 0601 UTC are employed to replace the original d02 of WRF. WRF is then allowed to run for another 2 h until 0801 UTC. Figure 18 compares the predicted 2-h (0601–0801 UTC) accumulated rainfall distribution from experiment OBS_EC (a pure VDRAS simulation based on a background field prepared from in situ measurements and ECMWF data), experiment WRF (a pure WRF simulation without the replacement of d02), and experiment OBS_EC+WRF (merging WRF with VDRAS) against the observations. The observed rainfall pattern, shown in Fig. 18a, indicates that the areas of heavy precipitation are in the southwestern plain, southern tip, and central part of Taiwan. These features are well captured by experiments OBS_EC

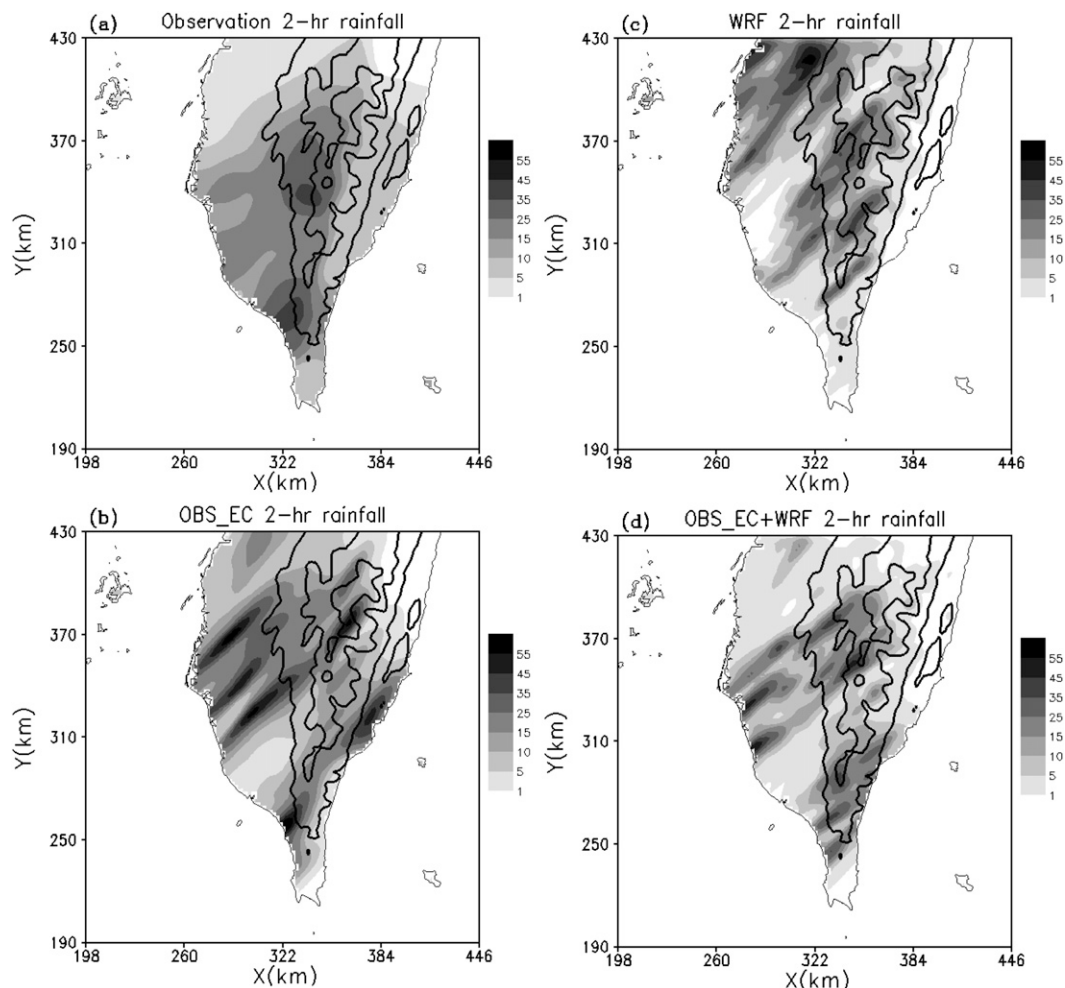


FIG. 17. The 2-h accumulated rainfall amount (shading at 5- and 10-mm intervals) for case 1 (IOP 8) from (a) rain gauge observations, (b) experiment OBS_EC, (c) experiment WRF, and (d) experiment OBS_EC+WRF. The thick solid lines depict the terrain heights at 500, 1500, and 2500 m.

and OBS_EC+WRF, but missed by experiment WRF. Moreover, it is obvious that experiments OBS_EC and WRF tend to overpredict the rainfall amount over the mountainous regions as well as in the eastern part of Taiwan. A quantitative comparison is provided in Fig. 19, in which the ETS scores for the forecasted total precipitation are depicted. It is clear that OBS_EC+WRF outperforms WRF and OBS_EC at all rainfall thresholds. The ETS scores produced by OBS_EC+WRF for the 10 and 14 mm $(2 \text{ h})^{-1}$ thresholds can reach 0.406 and 0.481, respectively. In contrast, the ETS scores from the pure VDRAS simulation (i.e., experiment OBS_EC) are only about 0.30 or below.

Finally, in an attempt to examine how long the influence from combining VDRAS with WRF can be retained, the hourly ETS scores from 0601 to 0901 UTC are also computed for this case. It is found that experiment OBS_EC+WRF has better QPF capability than

experiment WRF within the first 2 h (i.e., 0601–0701 and 0701–0801 UTC). For example, for the 6 and 10 mm $(2 \text{ h})^{-1}$ rainfall thresholds, the ETSs from experiment OBS_EC+WRF are about 0.20–0.25, while those from experiment WRF are less than 0.075. However, during the third hour (0801–0901 UTC), the ETS scores for both experiments OBS_EC+WRF and WRF begin to exhibit similarity, but they all drop dramatically to about 0.05 or lower. This result implies that at least for this particular case study, the positive impact from merging VDRAS with WRF can be maintained for approximately 2 h.

9. Summary and future work

In this research the QPF capability of VDRAS in Taiwan and vicinity is investigated. The complex topography of Taiwan poses a great challenge, since VDRAS is formulated over a flat surface. In addition, the oceans

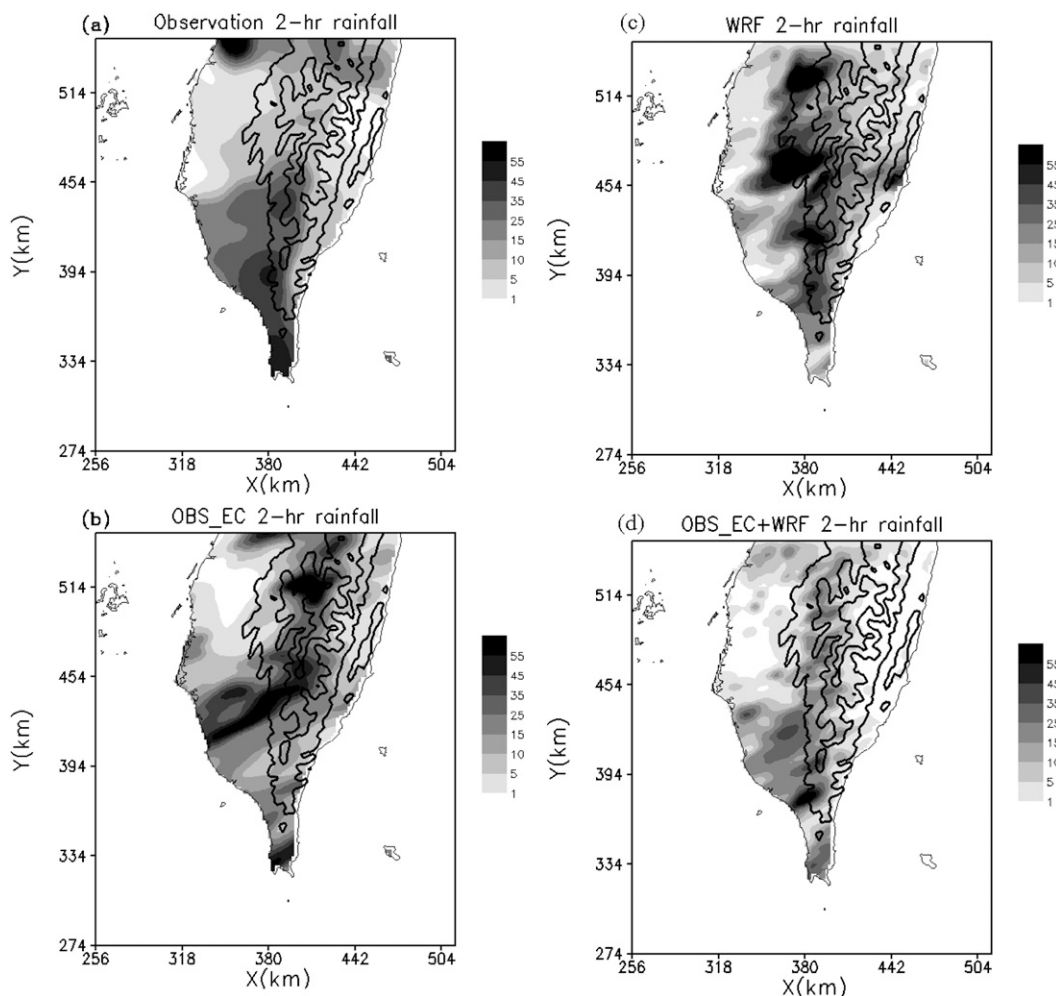


FIG. 18. As in Fig. 17, but for case 2 (IOP 4).

surrounding the island also create a serious constraint to the deployment of in situ instruments. As a result, the role played by radar becomes extremely vital. Two real cases observed during IOPs 4 and 8 of the 2008 SoWMEX are selected for this study. Our major findings are listed below.

- (i) The analysis kinematic and thermodynamic characteristics retrieved by the VDRAS 4DVAR technique are quite reasonable. These fields can reflect the topographic effects, even though VDRAS does not explicitly resolve the terrain.
- (ii) The VDRAS forecasts are sensitive to the background fields. An appropriate strategy to prepare the background field is to combine in situ measurements over the land and the reanalysis data (or an output from another mesoscale model) over the oceans.
- (iii) The accuracy of the rainfall forecast can be significantly improved by merging the VDRAS

analysis fields with the WRF. The ETS values at different precipitation thresholds obtained by combining VDRAS and WRF are generally much better than those obtained from using VDRAS or WRF alone. This can be attributed to the assimilation of meso- and convective-scale information, embedded in the radar data, into VDRAS, and to

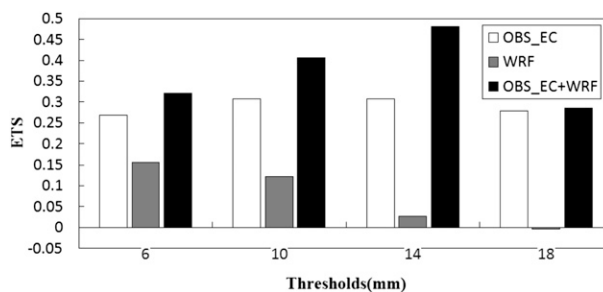


FIG. 19. As in Fig. 16, but for case 2 (IOP 4).

the appropriate treatment of topographic effects during WRF simulation. However, the case examined in this study indicates that the positive impacts of merging VDRAS with WRF can be maintained for about 2 h.

- (iv) This study demonstrates a feasible extension for applying VDRAS in other regions with geographic conditions and observational limitations that are similar to those in the Taiwan area.
- (v) In the future, the VDRAS analysis domain would be extended to include data from more radars in the computation. We also plan to modify its microphysical scheme by adding the ice phase into the algorithm. Finally, an ongoing task is to implement the terrain-resolving capability into VDRAS, so that this system can be run directly over complex terrain.

Acknowledgments. The comments from three anonymous reviewers are highly appreciated. The authors are very grateful to the SoWMEX project team. This research is supported by the National Science Council of Taiwan, under Grants NSC99-2625-M-008-001, NSC99-2111-M-008-003, NSC100-2625-M-008-002, and NSC100-2111-M-008-005, and the Central Weather Bureau of Taiwan, under Grant MOTC-CWB-99-2M-02.

REFERENCES

- Brewster, K. A., 2003: Phase-correction data assimilation and application to storm-scale numerical weather prediction. Part I: Method description and simulation testing. *Mon. Wea. Rev.*, **131**, 480–492.
- Chien, F.-C., and Y.-H. Kuo, 2006: Topographic effects on a wintertime cold front in Taiwan. *Mon. Wea. Rev.*, **134**, 3297–3315.
- , —, and M.-J. Yang, 2002: Precipitation forecast of MM5 in the Taiwan area during the 1998 mei-yu season. *Wea. Forecasting*, **17**, 739–754.
- Chung, K.-S., I. Zawadzki, M. K. Yau, and L. Fillion, 2009: Short-term forecasting of a midlatitude convective storm by the assimilation of single-Doppler radar observations. *Mon. Wea. Rev.*, **137**, 4115–4135.
- Clark, A. J., W. A. Gallus Jr., M. Xue, and F. Kong, 2009: A comparison of precipitation forecast skill between small convective-allowing and large convection-parameterizing ensembles. *Wea. Forecasting*, **24**, 1121–1140.
- Crook, N. A., 1994: Numerical simulations initialized with radar-derived winds. Part I: Simulated data experiments. *Mon. Wea. Rev.*, **122**, 1189–1203.
- , and J. D. Tuttle, 1994: Numerical simulations initialized with radar-derived winds. Part II: Forecasts of three gust-front cases. *Mon. Wea. Rev.*, **122**, 1204–1217.
- , and J. Sun, 2002: Assimilating radar, surface, and profiler data for the Sydney 2000 Forecast Demonstration Project. *J. Atmos. Oceanic Technol.*, **19**, 888–898.
- Gal-Chen, T., 1978: A method for the initialization of the anelastic equations: Implications for matching models with observations. *Mon. Wea. Rev.*, **106**, 587–606.
- Gao, J., K. Brewster, and M. Xue, 2006: A comparison of the radar ray path equations and approximations for use in radar data assimilation. *Adv. Atmos. Sci.*, **23**, 190–198.
- Hong, J.-S., 2003: Evaluation of the high-resolution model forecasts over the Taiwan area during GIMEX. *Wea. Forecasting*, **18**, 836–846.
- Hu, M., M. Xue, J. Gao, and K. Brewster, 2006a: 3DVAR and cloud analysis with WSR-88D level-II data for the prediction of the Fort Worth, Texas, tornadic thunderstorms. Part I: Cloud analysis and its impact. *Mon. Wea. Rev.*, **134**, 675–698.
- , —, —, and —, 2006b: 3DVAR and cloud analysis with WSR-88D level-II data for the prediction of the Fort Worth, Texas, tornadic thunderstorms. Part II: Impact of radial velocity analysis via 3DVAR. *Mon. Wea. Rev.*, **134**, 699–721.
- Jung, Y., G. Zhang, and M. Xue, 2008a: Assimilation of simulated polarimetric radar data for a convective storm using the ensemble Kalman filter. Part I: Observation operators for reflectivity and polarimetric variables. *Mon. Wea. Rev.*, **136**, 2228–2245.
- , M. Xue, G. Zhang, and J. M. Straka, 2008b: Assimilation of simulated polarimetric radar data for a convective storm using the ensemble Kalman filter. Part II: Impact of polarimetric data on storm analysis. *Mon. Wea. Rev.*, **136**, 2246–2260.
- Kain, J. S., and Coauthors, 2010: Assessing advances in the assimilation of radar data and other mesoscale observations within a collaborative forecasting-research environment. *Wea. Forecasting*, **25**, 1510–1521.
- Kessler, E., 1969: *On the Distribution and Continuity of Water Substance in Atmospheric Circulation*. Meteor. Monogr., No. 32, Amer. Meteor. Soc., 84 pp.
- Koizumi, K., Y. Ishikawa, and T. Tsuyuki, 2005: Assimilation of precipitation data to the JMA mesoscale model with a four-dimensional variational method and its impact on precipitation forecasts. *SOLA*, **1**, 45–48.
- Kong, F., and Coauthors, 2009: A real-time storm-scale ensemble forecast system: 2009 spring experiment. Preprints, *23rd Conf. on Weather Analysis and Forecasting/19th Conf. on Numerical Weather Prediction*, Omaha, NE, Amer. Meteor. Soc., 16A.3. [Available online at <http://ams.confex.com/ams/pdfpapers/154118.pdf>.]
- Lee, W.-C., B. J.-D. Jou, C. R. Chen, and J. A. Moore, 2009: Overview of SoWMEX/TiMREX. Preprints, *34th Conf. on Radar Meteorology*, Williamsburg, VA, Amer. Meteor. Soc., 9B.2. [Available online at <http://ams.confex.com/ams/pdfpapers/156254.pdf>.]
- Lin, Y., P. Ray, and K. Johnson, 1993: Initialization of a modeled convective storm using Doppler radar-derived fields. *Mon. Wea. Rev.*, **121**, 2757–2775.
- Lin, Y.-L., R. D. Farley, and H. D. Orville, 1983: Bulk parameterization of the snow field in a cloud model. *J. Appl. Meteor.*, **22**, 1065–1092.
- Nakamura, H., K. Koizumi, and N. Mannoji, 2004: Data assimilation of GPS precipitable water vapor into the JMA mesoscale numerical weather prediction model and its impact on rainfall forecasts. *J. Meteor. Soc. Japan*, **82B**, 441–452.
- Rogers, E., T. L. Black, D. G. Deaver, G. J. DiMego, Q. Zhao, M. Baldwin, N. W. Junker, and Y. Lin, 1996: Changes to the operational “early” Eta analysis/forecast system at the National Centers for Environmental Prediction. *Wea. Forecasting*, **11**, 391–412.
- Saito, K., and Coauthors, 2006: The operational JMA non-hydrostatic mesoscale model. *Mon. Wea. Rev.*, **134**, 1266–1298.
- Schaefer, J. T., 1990: The critical success index as an indicator of warning skill. *Wea. Forecasting*, **5**, 570–575.

- Snyder, C., and F. Zhang, 2003: Assimilation of simulated Doppler radar observations with an ensemble Kalman filter. *Mon. Wea. Rev.*, **131**, 1663–1677.
- Sun, J., 2005: Initialization and numerical forecasting of a supercell storm observed during STEPS. *Mon. Wea. Rev.*, **133**, 793–813.
- , and N. A. Crook, 1997: Dynamic and microphysical retrieval from Doppler radar observations using a cloud model and its adjoint. Part I: Model development and simulated data experiments. *J. Atmos. Sci.*, **54**, 1642–1661.
- , and —, 2001: Real-time low-level wind and temperature analysis using single WSR-88D data. *Wea. Forecasting*, **16**, 117–132.
- , and Y. Zhang, 2008: Analysis and prediction of a squall line observed during IHOP using multiple WSR-88D observations. *Mon. Wea. Rev.*, **136**, 2364–2388.
- , M. Chen, and Y. Wang, 2010: A frequent-updating analysis system based on radar, surface, and mesoscale model data for the Beijing 2008 Forecast Demonstration Project. *Wea. Forecasting*, **25**, 1715–1735.
- Tong, M., and M. Xue, 2005: Ensemble Kalman filter assimilation of Doppler radar data with a compressible nonhydrostatic model: OSS experiments. *Mon. Wea. Rev.*, **133**, 1789–1807.
- Warner, T., E. A. Brandes, J. Sun, D. N. Yates, and C. K. Mueller, 2000: Prediction of a flash flood in complex terrain. Part I: A comparison of rainfall estimates from radar, and very short range rainfall simulations from a dynamic model and an automated algorithmic system. *J. Appl. Meteor.*, **39**, 797–814.
- , and Coauthors, 2007: The Pentagon shield field program—Toward critical infrastructure protection. *Bull. Amer. Meteor. Soc.*, **88**, 167–176.
- Weygandt, S. S., A. Shapiro, and K. K. Droegemeier, 2002: Retrieval of model initial fields from single-Doppler observations of a supercell thunderstorm. Part II: Thermodynamic retrieval and numerical prediction. *Mon. Wea. Rev.*, **130**, 454–476.
- Xiao, Q., and J. Sun, 2007: Multiple radar data assimilation and short-range QPF of a squall line observed during IHOP_2002. *Mon. Wea. Rev.*, **135**, 3381–3404.
- , Y.-H. Kuo, J. Sun, W.-C. Lee, E. Lim, Y. Guo, and D. M. Barker, 2005: Assimilation of Doppler radar observations with a regional 3DVAR system: Impact of Doppler velocities on forecasts of a heavy rainfall case. *J. Appl. Meteor.*, **44**, 768–788.
- Xue, M., M. Tong, and K. K. Droegemeier, 2006: An OSSE framework based on the ensemble square root Kalman filter for evaluating impact of data from radar networks on thunderstorm analysis and forecast. *J. Atmos. Oceanic Technol.*, **23**, 46–66.
- Yang, M.-J., B. J.-D. Jou, S.-C. Wang, J.-S. Hong, P.-L. Lin, J.-H. Teng, and H.-C. Lin, 2004: Ensemble prediction of rainfall during the 2000–2002 Mei-yu seasons: Evaluation over the Taiwan area. *J. Geophys. Res.*, **109**, D18203, doi:10.1029/2003JD004368.
- , D.-L. Zhang, and H.-L. Huang, 2008: A modeling study of Typhoon Nari (2001) at landfall. Part I: Topographic effects. *J. Atmos. Sci.*, **65**, 3095–3115.
- Zhao, Q., J. Cook, Q. Xu, and P. R. Harasti, 2006: Using radar wind observations to improve mesoscale numerical weather prediction. *Wea. Forecasting*, **21**, 502–522.